Surrogate Modeling of Lithium-Ion Battery Electrode Manufacturing by Combining Physics-Based Simulation and Deep Learning

Utkarsh Vijay, Francisco Fernandez, Siwar Ben Hadj Ali, Mark Asch, and Alejandro A. Franco*

Optimizing the manufacturing process of Lithium-Ion Batteries (LIB. Finding efficient approaches that accelerate and replace time-consuming, material scrap-expensive trials-and-error optimization methods is a key area of research. This work presents a comprehensive LIB electrode manufacturing framework that combines physics-based simulations with deep learning. This framework efficiently simulates the manufacturing process of LIB electrodes as a function of their formulation. This framework takes the form of a surrogate manufacturing model able to predict the impact of manufacturing parameters on the electrode microstructure and properties. The model is based on a regressor-inspired variational autoencoder method. The analysis of the data and the predicted electrode functional metrics demonstrates the consistency of the approach with an electrode manufacturing model developed on the basis of physics. The reported framework holds significant promise in paving near real time optimization of LIB electrode manufacturing and supporting the optimization of battery cell design in pilot lines.

1. Introduction

The ultimate Lithium-Ion Battery (LIB) performance is influenced by its manufacturing process. By refining process parameters, manufacturers can minimize waste, improve scalability, and lower energy consumption, leading to more cost effective and environmentally friendly production.[1] This process involves many complex steps, such as slurry mixing, coating and drying, calendering, cell assembly, degassing, and electrolyte infiltration. All these steps directly influence the LIB electrode microstructure, and consequently, the electrochemical performance and lifespan of the cell.[2,3] While optimizing each one of these steps, we can find numerous process parameter variabilities, including slurry formulation, slurry drying rate, and pressure along the electrode calendering, among others. A proper optimization of these parameters is essential for producing optimized electrodes while reducing waste and enhancing overall sustainability.[4]

While empirical methods are widely used for optimizing electrode manufacturing and validating LIB cell performance, they can be time-consuming and resource intensive.[5–8] In contrast, physics-based computational simulations can provide accurate and reliable outcomes that help to understand the relationship between the electrode microstructure and its manufacturing. These models can capture physicochemical interactions at multiple scales, enabling predictive analysis, process and design optimization along the different stages of the manufacturing process.[9–13]

With the advancement in the field of data-driven science,[14–16] these physics-based simulations can be integrated with cutting-edge tools, such as Artificial Intelligence (AI), Machine Learning (ML), and Deep Learning (DL), to overcome the associated computational cost by maintaining a high accuracy and reliability.[17,18] By leveraging AI-based models within battery manufacturing workflows, real-time adjustments can be made to improve consistency, reduce defects, and enhance overall optimization process by deconvoluting the link between manufacturing parameters and the final microstructure and

U. Vijay, F. Fernandez, S. Ben Hadj Ali, A. A. Franco
Laboratoire de Réactivité et de Chimie des Solides
UMR CNRS 7314
Université de Picardie Jules Verne
F-80039 Amiens Cedex 1, France
E-mail: alejandro.franco@u-picardie.fr

U. Vijay, S. Ben Hadj Ali, A. A. Franco
ALISTORE-European Research Institute
FR CNRS 3104
Hub de l'Energie
15 rue Baudelocque, 80039 Amiens Cedex, France

F. Fernandez, S. Ben Hadj Ali, A. A. Franco
Réseau sur le Stockage Electrochimique de l'Energie (RS2E)
FR CNRS 3459
Hub de l'Energie
15 rue Baudelocque, 80039 Amiens Cedex, France

M. Asch
LAMFA
CNRS UMR 7352
Université de Picardie Jules Verne
33 rue Saint Leu, 80039 Amiens, France

A. A. Franco
Institut Universitaire de France
103 Boulevard Saint Michel, 75005 Paris, France

Batteries & Supercaps

Research Article
doi.org/10.1002/batt.202500433

Chemistry Europe

European Chemical
Societies Publishing

performance of the electrode.[19] However, integrating these advanced methodologies into existing physical manufacturing processes is challenging due to factors such as experimental data availability, model and experimental data interpretability, and the complexity of interactions between process steps.[20] Therefore, developing a robust surrogate manufacturing framework that combines physics-based simulation with AI-driven models is essential to overcoming these challenges and driving the future of intelligent, efficient, and adaptable battery manufacturing and related optimization solutions.[17,18,21–24]

Lombardo et al. from our group,[25] used physics-based simulations combined with AI-inspired optimization techniques to study the electrode slurry phase in LIB manufacturing. They leveraged Coarse-Grained Molecular Dynamics (CGMD) and particle swarm optimization for force field parameterization, allowing to simulate electrode slurry microstructures that were further validated experimentally. Similarly, Malki et al. also from our group,[26] proposed an ML workflow to study electrode filling by a liquid electrolyte, establishing a synthetic map linking electrolyte properties and filling conditions with the electrode wettability. This work involved creating and evaluating 250 distinct parameter sets using a Lattice Boltzmann method model. Then, it was found that low viscosity, high pressure, and a good contact angle favor optimal impregnation. Finegan et al.[27] highlighted the potential of generative AI techniques for integrating multimodal datasets in LIB electrode characterization, overcoming limitations that are present in experimental techniques. While data-driven models are good at finding complex patterns and are often faster to run (except for the training of supervised methods), they can struggle to perform well when faced with new or unseen conditions. With tools like generative AI, one can create electrode microstructures digitally.[28] However, these AI models can still face challenges, especially when data availability is limited, when process variables interact in nonlinear or high-dimensional ways, or when the training data fails to capture rare or edge-case scenarios. In contrast, physics-based models are built on the fundamental physical laws of the process, which makes them better for explainability and at predicting results outside of known scenarios. Our ARTISTIC research initiative originated mesoscale physics-based simulators and AI/ML/DL models of the entire manufacturing process, from powder to power. The ARTISTIC approach allows providing holistic understanding on how manufacturing process parameters impact slurry, electrode, and cell properties.[29]

In our previous work,[33] we demonstrated the advantages of a hybrid approach by coupling physics-based CGMD simulations with DL for the slurry stage. The approach enhanced prediction accuracy, captured complex structure–property relationships, and demonstrated reliable agreement with key microstructural metrics, such as porosity, spatial distribution, and rheological properties, across different electrode chemistries. In the context of LIB manufacturing, Prof. Franco's group has highlighted that hybrid approaches combine the strengths of both worlds, the interpretability and extrapolatibility power of physics-based models, together with the pattern recognition, adaptability,

and computational efficiency of data-driven methods.[29] These approaches have been explored to enhance battery cell manufacturing and facilitate the transition from research outputs to industrial applications.[29]

In this work, we introduce a novel hybrid manufacturing modeling workflow that integrates physics-based simulations with DL predictions across multiple stages of the electrode fabrication process, specifically slurry preparation and drying. This integrated approach enables accurate prediction of the dried electrode microstructure directly from slurry formulation, significantly enhancing computational efficiency and generalizability. Electrode manufacturing is a highly complex process involving multiple stages, multiple objectives (for e.g., optimal porosity and low tortuosity factor), and scales. Because of this complexity, physics-based models are valuable for generating realistic data without relying solely on costly and time-consuming post-manufacturing experiments to create training datasets.[30–32] Building on this, we first acquire data from physics-based simulations of the drying step, as illustrated by the red arrow in **Figure 1**, and use it to train a Neural Network (NN), which is discussed in detail in the following section, to predict the dried electrode microstructure. Then, this model is linked to the slurry NN from our previous work[33] to predict the dried electrode microstructure within a workflow fully based on NN predictions, as indicated in blue in Figure 1. Finally, the electrochemical performance is evaluated after a calendering simulation for both electrodes, one generated from the physics-based approach and the other from the NN-based workflow, and the results are compared. The following sections outline the dataset generation, the DL model architecture and training, followed by results and discussion, conclusions, and indication of future work.

2. Experimental Section

2.1. Drying-NN Workflow

Herein, we propose to model the slurry drying step using a NN, referred to as Drying-NN, that uses a regressor-inspired Variational Autoencoder (VAE). We designed this framework to predict dried electrode microstructures using particle coordinates obtained from time-dependent physics-based simulations.[34] As illustrated in **Figure 2**, the framework begins with the encoding process of the input parameters (X), in this case, the particle coordinates. The encoder generates the mean (μ_x) and standard deviation (σ_x) of the latent distribution. For deterministic prediction, the latent variable is set to $Z = \mu_x$, bypassing the traditional sampling step typical in VAEs. This latent variable ($Z = \mu_x$) is then passed to the decoder, which generates the predicted output (Y), here the updated particle coordinates representing the final dried porous electrode microstructure. This approach integrates both physics-based simulations and data-driven DL techniques, efficiently modeling and predicting the electrode microstructure, balancing accuracy and computational efficiency. While structurally similar to a VAE, this model does not function as a traditional generative model. Instead, it focuses on using the latent variables for representation learning, rather than generating new data samples.[35]
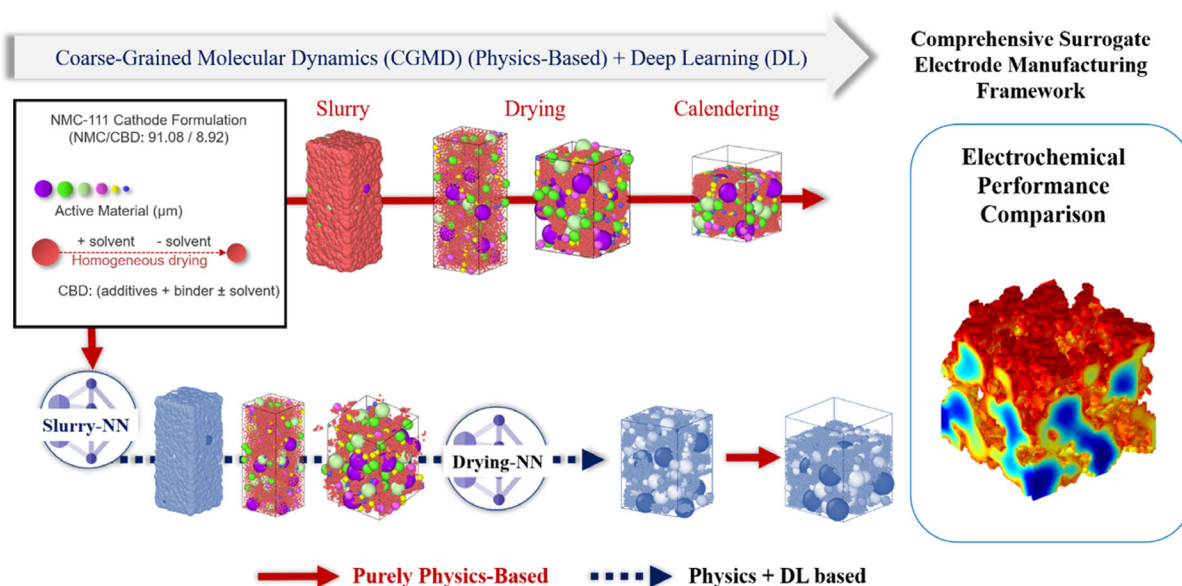
Batteries & Supercaps

Research Article
doi.org/10.1002/batt.202500433

Chemistry Europe
European Chemical
Societies Publishing

Figure 1. Schematic of our comprehensive hybrid manufacturing modeling workflow for LIB electrodes. The workflow integrates physics-based simulations (indicated by red arrows), based on CGMD, and DL predictions (indicated by blue arrows) at multiple manufacturing stages to predict the final dried porous electrode microstructure. It also includes calendering and electrochemical simulations used to assess and compare the quality and performance of electrode microstructures generated by both the physics-based and hybrid (DL + Physics) based workflows.
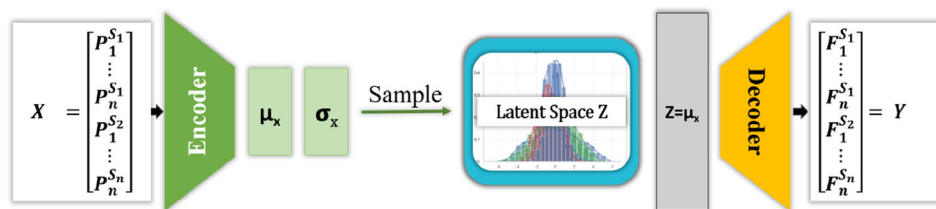

Figure 2. Workflow of our Variational Autoencoder (VAE) framework for LIB electrode manufacturing modeling. The encoder processes input parameters (X) to generate the latent variable ($Z = \mu_x$), which is then passed to the decoder to predict the output matrix (Y), representing the final dried porous electrode microstructure. The meaning of the different variables is provided in the manuscript text.

2.2. Preprocessing of Data into a Dataset

Previously, Ngandjong et al.[10] part of our ARTISTIC group, conducted slurry drying simulations using the final slurry microstructure obtained by CGMD. Following similar steps, for the physics-based computational part of our work, we generated 3D slurry microstructures for nickel manganese cobalt oxide (NMC-111) as an Active Material (AM) and further simulated their drying in order to obtain the dried electrode microstructures. In the slurry modeling, we consider two types of particles: AM and Carbon Binder Domain (CBD) with solvent. The CBD represents effective particles comprising conductive carbon black, polyvinylidene fluoride binder, and N-methylpyrrolidone.

These generated microstructures were used as a time series representation of microstructural evolutions to construct the training dataset. Each dataset sample consisted of particle attributes, including the particle's unwrapped coordinates (i.e., the raw positions of particles without any periodic transformation)[36] from the first three steps (as input features), used to forecast the future unwrapped coordinates of the dried electrode microstructure (as the target). Along with these unwrapped coordinates, denoted as xu, yu, and zu, we also include the particle type (t), and the particle mass (m). The input unwrapped coordinates follow a time series arranged for different time steps as Δ_{t-3}, Δ_{t-2}, and Δ_{t-1}. The output dataset consists of the particle's unwrapped coordinates from the last frame (Δ_t), which defines the dried electrode microstructure. **Figure 3**a,b, shows the matrix representation of the described input (X) and output (Y) attributes in the datasets, respectively. Figure 3c shows the dried electrode microstructures with both wrapped and unwrapped coordinates. The latter were used to enforce Periodic Boundary Conditions (PBCs), because our earlier studies showed that wrapped coordinates caused abrupt position jumps when particles crossed boundaries, leading to outliers.[33] Using unwrapped coordinates ensures smooth and accurate trajectory tracking, making similar displacement predictions for all particles, which will be further discussed in the Results Section.

Simulations were performed using the Large-scale Atomic/Molecular Massively Parallel Simulator (LAMMPS) software.[36] The simulation setup for the slurry drying step followed a similar configuration as described in the work done by Vijay et al.[33] including the same force fields and corresponding parameter values. The overall simulation workflow, including slurry, drying, and calendering, was carried out on the MatriCS HPC platform at Université de Picardie Jules Verne (Amiens, France). The calculations were executed in a single node equipped with 128 GB of RAM and two Intel Xeon CPU E5−2680 v4 processors, each featuring 14 cores @ 2.40 GHz (**Table 1**).
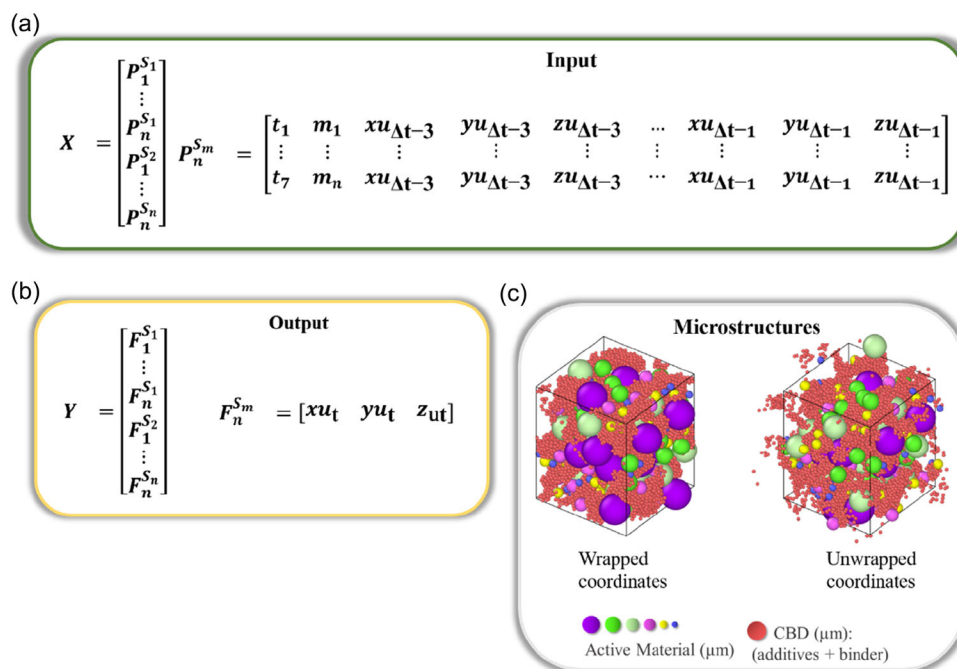
Figure 3. a) Matrices of the input parameters with simulation information, each row corresponds to the initial three frames of information for a specific particle, organized by the mth simulation (S_m) and particle n-index (P_n). $S_{(m = 0 \to 20)}$ represents the mth simulation and xu, yu, and zu denote the unwrapped particle coordinates. b) Target matrix containing output particle coordinates. c) The final microstructure with wrapped and unwrapped coordinates. The meaning of the different variables is provided in the manuscript text.

Table 1. Summary of the simulation configuration for data generation.

Parameters per simulation	NMC-111 (30 simulation)	Description
Timestep (μs)	0.001	Δt to update the positions
Total steps	69,000,000	Total number of iterations
Simulation time (μs)	69,000	Total duration of the simulation
Frames storage interval	62,500	Steps at which coordinates are recorded
Frames storage interval (μs)	0.0598	Intervals at which coordinates are recorded
Total number of frames	1154	Coordinates are printed at specified frame storage interval
Wall time (hrs.)	54	Total MD simulation time. This depends on computational resources available.

2.3. Model Architecture and Training

The Drying-NN contains the following components: the input attributes are passed to a Long Short-Term Memory (LSTM) layer to capture the temporal dependencies in the sequence data, followed by an attention layer to focus on the most relevant time steps. Fully connected layers then are responsible for calculating the latent variables (μ and σ^2), which are used for generating the latent representation. The decoder, consisting of dense layers, reconstructs the deterministic output, which are the predicted particle coordinates corresponding to the final timestep (xu_t, yu_t, and zu_t). **Figure 4** illustrates the architecture of the Drying-NN. To obtain the reported hyperparameters, we performed Bayesian optimization, since exhaustive grid-search would be too time consuming. More details are given in Table S1, Supporting Information.

The dataset was split into three subsets: 80% for training, 10% for validation, and 10% for testing. The testing dataset refers to data that was not used during the training or validation steps, making it a set that Drying-NN has not seen before, but it was still part of the original global dataset. The Drying-NN was trained using Huber loss Equation (1).

$$L_\delta(y, \hat{y}) = \begin{cases} \frac{1}{2}(y - \hat{y})^2, & \text{if } |y - \hat{y}| \leq \delta \\ \delta\left(|y - \hat{y}| - \frac{1}{2}\delta\right), & \text{if } |y - \hat{y}| > \delta \end{cases} \quad (1)$$

which combines the benefits of Mean Squared Error (MSE) for smaller errors and Mean Absolute Error (MeanAE) for larger errors, making it less sensitive to outliers. In Equation (1), $L_\delta(y, \hat{y})$ is the Huber loss for actual value y and predicted value $\hat{y}$, the residual is $y - \hat{y}$ (error between actual and predicted), and δ is the threshold parameter that controls the transition between MSE and MeanAE. Additionally, the R^2 score was used at the end of the training process as a measure of its predictive accuracy. Furthermore, R^2, MSE, MeanAE, and Median Absolute Error (MedianAE),[33,37] were also calculated for the unseen test data to evaluate the Drying-NN's generalization performance and its ability to predict accurately on new, unseen formulations.
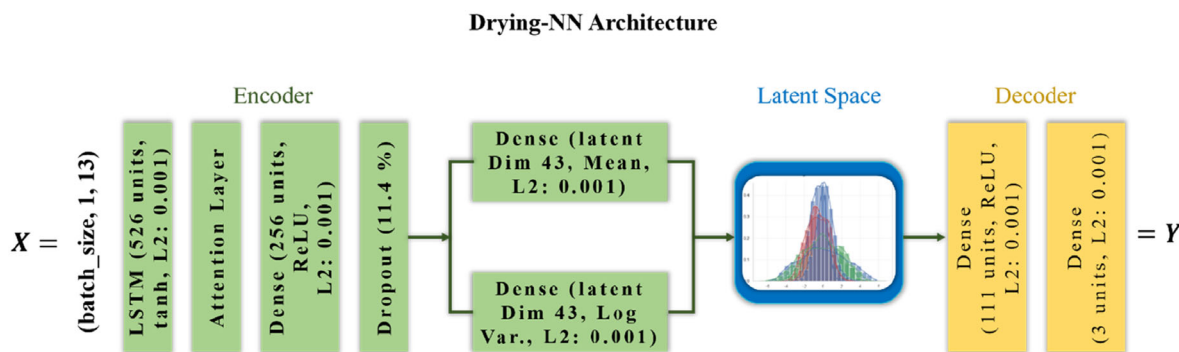
Drying-NN Architecture

Figure 4. Architecture of the NN for the drying step (Drying-NN) model, showing the data flow from input through the encoder, latent space, and decoder to generate the deterministic prediction of the dried electrode microstructure.

3. Results

3.1. Drying-NN Data Metrics

The Drying-NN was trained using the Huber loss, as described in the Methodology Section. The best training loss was 0.328, and the validation loss was slightly lower at 0.326, suggesting that it did not overfit and generalized well to the validation dataset. The close proximity of the training and validation losses (shown in Figure S1 of the Supporting Information) further supports its robustness. Following training, Drying-NN was evaluated on a completely unseen test dataset, distinct from both training and validation data. The model achieved an R^2 score of 0.996, capturing 99.6% of the variance in the target variable, indicative of near-perfect predictive accuracy. Based on the data metrics, the MSE was 0.445, indicating a moderate level of discrepancy between the predicted and the target values, when compared to training and validation values. The MeanAE was 0.503, reflecting an average deviation of ≈0.5 units from the target values. The MedianAE was 0.396, showing that half of the predictions had an error below 0.396 units. Overall, these results suggest the model performs reasonably well with relatively small prediction errors. However, there is room for improvement, particularly in reducing larger deviations and optimizing accuracy. Additionally, when applied to unseen electrode formulations, Drying-NN achieved an average R^2 of 0.971, demonstrating its generalization capability in predicting microstructures from physics-based data. **Figure 5** shows the predicted versus the target values for the testing dataset and for new unseen electrode formulations.

In Figure 5a, the data points align closely along the perfect prediction line (ideal prediction line), reflecting strong predictive performance for the formulation that the Drying-NN model was trained on. This is supported also by the previously mentioned high R^2 score, and the other data metrics. Figure 5b presents this same comparison for completely unseen datasets, referring to seven new simulations with different electrode formulations. Separate plots corresponding to each direction can be found in the Section S2 of the Supporting Information. For this case, we can appreciate some deviations from the ideal prediction line, however, the magnitude of these deviations is not unacceptably high. Along with this observation, **Table 2** presents high R^2 scores
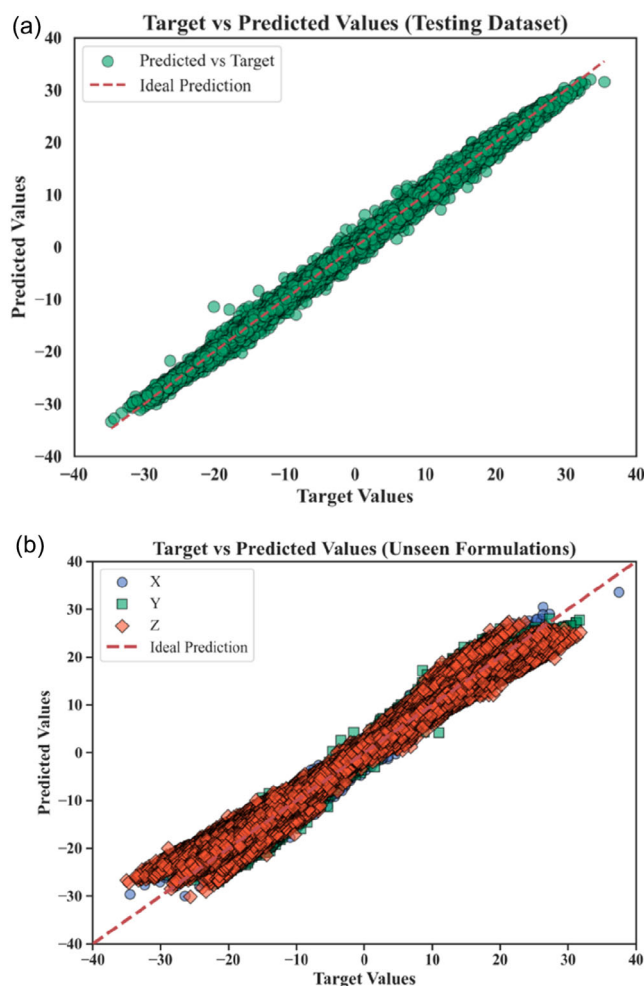

Figure 5. a) Comparison of target and predicted values for the testing dataset after training, showing a strong alignment along the perfect ideal prediction line. b) Comparison for unseen datasets, consisting of seven new simulations with different electrode formulations not used during the training, demonstrating the Drying-NN's generalizability.

with the other data metrics also in a reasonable range, suggesting that model generalizes well to new electrode formulations.

The MSE of 3.689 quantifies the overall magnitude of prediction error, while the MeanAE of 1.441 indicates that, on average,

Batteries & Supercaps

Research Article
doi.org/10.1002/batt.202500433

Chemistry
Europe
European Chemical
Societies Publishing

Table 2. R^2, MSE, MeanAE, and MedianAE evaluation of the Drying-NN on NMC-111 based cathode unseen formulations.

#	NMC-111/CBD	R^2	MSE	MeanAE	MedianAE
I	88.4:11.6	0.993	0.954	0.804	0.728
II	89.3:10.66	0.993	0.963	0.771	0.648
III	89.47:10.53	0.971	3.682	1.513	1.429
IV	93.55:6.45	0.942	7.942	2.312	2.238
V	93.63:6.37	0.971	3.880	1.621	1.517
VI	94.16:5.84	0.991	0.970	0.782	0.683
VII	94.85:5.15	0.933	7.429	2.285	2.172
	Average	0.971	3.689	1.441	1.345

the model's predictions deviate by 1.441 units from actual values. The MedianAE of 1.345, being less sensitive to outliers, further underscores the model's robustness. Notably, the model's robustness to outliers can be attributed to the use of unwrapped coordinates for enforcing PBCs. It can be observed that this approach reduces the abrupt coordinate jumps previously seen with

wrapped coordinates,[33] leading to more accurate predictions and enhancing the model's ability to generalize to unseen formulations.

3.2. Radial Distribution Function (RDF) of the Electrode Microstructures

Figure 6 presents the three microstructures and the Radial Distribution Function (RDF) of one of the unseen formulations [NMC-111/CBD: 88.4:11.6]. Figure 6a presents the geometrical arrangement of the target, the predicted, and the equilibrated microstructure. The later one being the predicted microstructure with an additional equilibration CGMD step over a time interval of $\Delta t = 0.001$, in the canonical ensemble (NVT). In the RDF curves of Figure 6b, the predicted microstructure exhibits peaks at the same locations as the target microstructure in the nearest neighbor's region. Nevertheless, these peaks have lower intensity and higher spread, which can be attributed to the dispersion of particle positions predicted by the Drying-NN. In contrast, the equilibrated microstructure is overlapped with the target one,
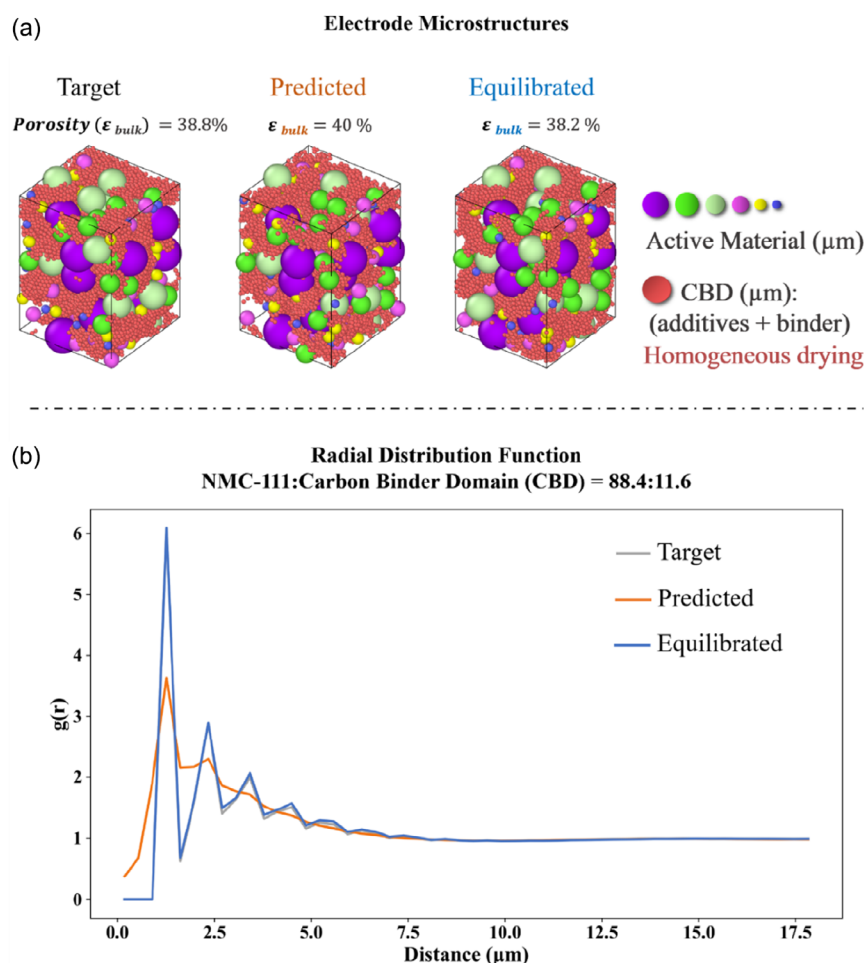

Figure 6. Comparison of the dried electrode microstructures (target, predicted, and equilibrated) and their RDF curves ($\Delta r_{RDF} = 0.36$) for an unseen formulation [NMC-111/CBD: 88.4:11.6]. a) Target, predicted, and equilibrated microstructure, the later corresponding to the predicted microstructure with an additional CGMD step over a time interval of $\Delta t = 0.001$ in the canonical ensemble (NVT). b) The RDF curves illustrating the spatial radial distribution of particles within each corresponding microstructure (target, predicted, and equilibrated microstructures).

Batteries & Supercaps

Research Article
doi.org/10.1002/batt.202500433

Chemistry Europe
European Chemical
Societies Publishing

indicating a more accurate representation of the particle distribution. This indicates that the Drying-NN model effectively captures structural radial features, and when coupled with physics-based simulation, it improves the accuracy in predicting microstructural arrangements. The RDFs corresponding to all the unseen formulations show similar results and are detailed in the Section S3 of the Supporting Information.

3.3. Electrode Functional Metrics

For further evaluation, the microstructures were voxelized (whose voxelizations are shown in **Figure 7**a), with a voxel size of 0.4 μm, using an in-house developed Python code.[17] Comparative evaluation was conducted by analyzing the transport properties of the voxelized microstructure: porosity (ε), tortuosity factor (τ), and conductivity (σ/σ_o), to assess the reliability of the equilibrated microstructure. The abovementioned properties were calculated following the methodology described in some of our previous works,[12,17,38,39] using the ConductoDict and DiffuDict modules of GeoDict 2024 (Math2Market).

Figure 7b presents the porosity of the three microstructures (target, predicted, and equilibrated) across each unseen formulation. The predicted microstructures exhibit slightly higher porosity than the target ones, likely due to subtle radial differences as observed in the RDF curves. However, in the equilibrated microstructure, porosity values improved, and are closer to those of the target microstructures, though they remain slightly lower. A similar trend was observed for the tortuosity factor, with the Drying-NN predicted microstructures initially exhibiting lower values than the target across most formulations (Figure 7c). Equilibrating the predicted microstructure shifted the tortuosity values closer to those of the target,
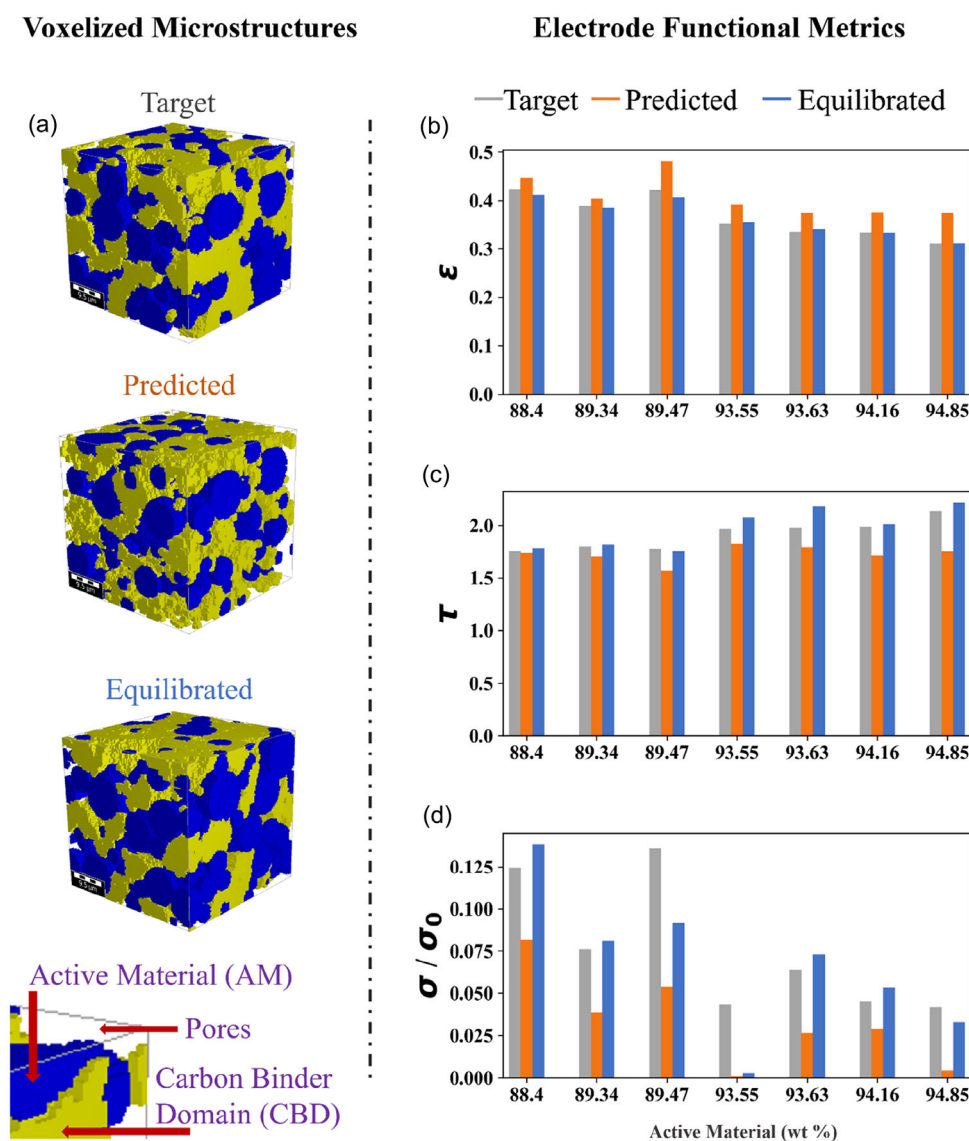

Figure 7. a) Voxelized images of the target, predicted, and equilibrated microstructures for [NMC-111/CBD: 88.4:11.6], with a voxel size of 0.4 μm. b) Porosity (ε), c) tortuosity factor (τ), and d) electrical conductivity (σ/σ_o) of the three microstructures across different formulations.

indicating a reduction in structural discrepancies and improving microstructural accuracy.

Similarly, for the electrical conductivity, in Figure 7d, the equilibrated microstructures show strong alignment with the target values across most formulations. In several cases, such as formulation NMC/CBD: 88.4:11.6 (target: 0.124, predicted: 0.081, equilibrated: 0.138) and 89.3:10.66 (target: 0.076, predicted: 0.038, equilibrated: 0.080), equilibration led to a notable improvement in microstructural accuracy compared to the predicted values. Although some deviation remains, particularly in the case of NMC/CBD 93.55:6.45, the overall results demonstrate that the Drying-NN model effectively captures electrical conductivity patterns. The equilibrated microstructures further enhance this performance, reinforcing the reliability of the predictive framework.

3.4. Comprehensive Simulation Framework

For validating the predictions of the Drying-NN, the electrochemical performance was evaluated through the discharge profiles obtained with the different microstructures. For this purpose, we reconstruct the full manufacturing chain, from its slurry to the calendered electrode, with both physics-based and DL modeling approaches. The comparison workflow is illustrated in Figure 1, where we first applied a traditional CGMD simulations

to generate a dried microstructure and performed calendering simulation at a 25% compression degree using Discrete Element Method (DEM), hereafter referred to as the physics-based microstructure. Similarly, we followed the same methodology but employed a physics-based and DL-integrated manufacturing chain to predict the dried electrode microstructure. First, we utilized our previous model, Slurry-NN,[33] to predict the slurry microstructure for formulation NMC-111/CBD: 91.08/8.92, as shown in Figure 1. This formulation was selected randomly from our dataset to demonstrate the methodology, rather than being chosen for a particular composition. The predicted slurry microstructure was then used as input for CGMD drying simulation to generate predictions using Drying-NN. Finally, the predicted microstructure underwent a calendering simulation at 25% compression degree by DEM simulation. It is noted here that for the DEM, the predicted microstructure did not undergo separate equilibration and is hereafter referred to as the predicted microstructure.

First, the porosity and tortuosity factor of the calendered electrodes were compared in **Table 3**. The results indicate that the porosity of the electrode generated by the physics-based simulator was 27.87%, whereas the porosity of the predicted electrode was slightly lower at 27.08%, representing a 2.83% decrease. Similarly, the tortuosity factor decreased marginally from 2.47 for the electrode originated by the physics-based simulator to 2.40 for the DL-predicted microstructure. Electrical conductivity also showed a decrease of 7.14%, from 0.14 to 0.13. These results suggest that the incorporation of the DL approach leads to a slightly denser and less tortuous electrode microstructure, with slight differences between the two microstructures.

Further, to assess the practical relevance of these microstructural changes, we conducted computational simulations of galvanostatic discharge of these microstructures. For this, the electrode microstructures were voxelized with a resolution of 0.4 μm and then meshed using INNOV,[40] an in-house developed

Table 3. Electrode properties after 25% calendering degree using different microstructure generation approaches.

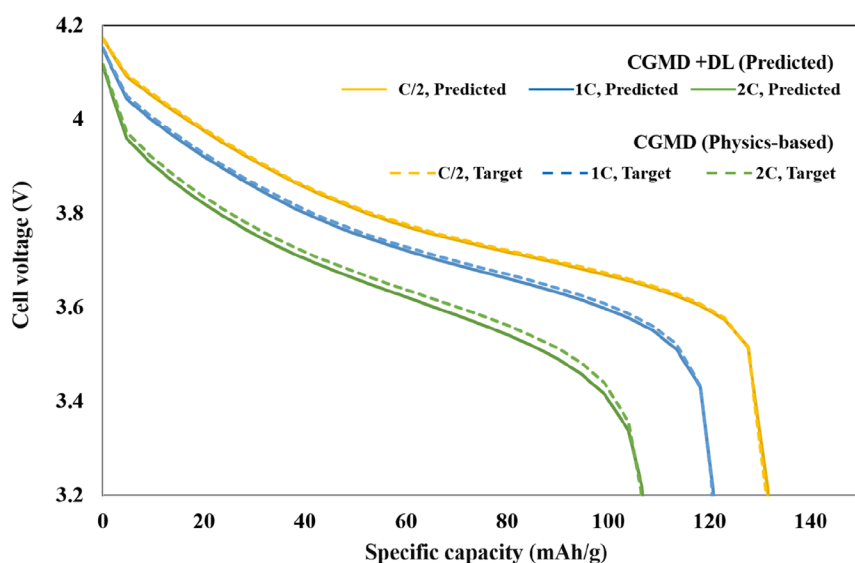| Properties	Calendered (25% degree)		
	Generated by the physics-based simulator	DL predicted	% error
Porosity (%)	27.87	27.08	2.83
Tortuosity factor	2.47	2.40	2.83
Conductivity (σ/σ_o)	0.14	0.13	7.14

Figure 8. Discharge profiles at different C-rates (C/2, 1C, and 2C) for electrodes predicted using CGMD (solid lines) and DL + CGMD (dashed lines).

Batteries & Supercaps

Research Article
doi.org/10.1002/batt.202500433

Chemistry
Europe
European Chemical
Societies Publishing

software designed for generating meshes for Finite Element Method (FEM) computations. COMSOL Multiphysics was employed as the FEM platform to generate the galvanostatic curves, following the parameters and methodology outlined in work done by Liu et al.[41] The equations and parameters for both FEM and electrochemical models are outlined in the tables of Section S4 of the Supporting Information. As can be observed in **Figure 8**, the electrode predicted by the hybrid approach (DL + CGMD) demonstrates a highly accurate electrochemical performance across varying C-rates. The calculated curves closely match the (physics-based) CGMD target data, with the highest agreement observed at the C/2 rate. The MeanAE between the predicted and target electric potential values was 0.004 V for the C/2 rate, 0.085 V for the 1C rate, and 0.016 V for the 2C rate. While slight deviations appear at higher C-rates, particularly at 1C and 2C and in the lower voltage region, the electrode microstructure arising from the hybrid model still offers good accuracy. Overall, this hybrid modeling approach shows excellent potential for accelerating simulations with minimal loss of accuracy, offering a reliable complement to pure physics-based computational methods for electrode manufacturing simulation.

4. Conclusions and Perspectives

In this work, we introduced an interlinked, comprehensive LIB electrode manufacturing modeling workflow. This workflow couples a physics-based simulation technique with DL models to predict final electrode microstructures. This approach was demonstrated to be generalizable to varying electrode formulations. We employed a VAE-inspired architecture, consisting of LSTM units, to train artificial NNs for predicting dried electrode microstructures based on NMC-111, serving as a proof-of-concept system. Based on the cathode formulations, slurry microstructures were first generated using a physics-based approach. These microstructures then underwent a simulated drying process, which produced temporal trajectory data. This data was then used as input for the Drying-NN model, which predicted the dried electrode microstructures. These microstructures were used to calculate the metrics (both data and functional electrode ones). The microstructures predicted by the DL architecture of the encoder and decoder showed strong agreement with the ground truth microstructures. Its accuracy further improved with an equilibration step, as evaluated using the RDF metric across the multiple formulations. While no significant differences were observed in porosity or tortuosity factor metrics for the dried electrodes, the variation in conductivity could be attributed to insufficient CBD connectivity because calendering was not performed at this stage. Along with the evaluation of Drying-NN, we also modeled a cathode microstructure using a comprehensive manufacturing framework that integrates DL models for the slurry and drying stages, using the herein developed Drying-NN and our previously developed Slurry-NN, followed by a calendering simulation using DEM. This framework was compared with a purely physics-based chain approach. The microstructures obtained with both approaches were electrochemically evaluated by simulating the discharge profiles at different C-rates. The evaluation demonstrated that the electrochemical performance of the microstructure predicted by the approach including the Slurry-NN and the Drying-NN aligned with that of the physics-based approach.

The LIB electrode manufacturing surrogate model presented in this study demonstrates strong consistency with the computations derived by CGMD. In the future, this work could be extended to enable the generation of multiple plausible electrode microstructures from a given formulation, allowing the model to account for the variability of more process parameters and support applications such as inverse design.[29,31,42] With access to experimental data, the developed model can be adapted to systematically investigate the impact of manufacturing formulations on LIB electrode microstructure and performance. While our approach was demonstrated with spherical representations of the AM particles, it can be adapted to address nonspherical and deformable particles by leveraging our previously reported physics-based electrode manufacturing models.[43,44] This interdisciplinary and innovative approach proposed in this article provides an efficient and scalable methodology for optimizing electrode design and advancing battery manufacturing.

Supporting Information

The authors have cited additional references within the Supporting Information.[45–51]

Conflict of Interest

The authors declare no conflict of interest.

Data Availability Statement

The data that support the findings of this study are available from the corresponding author upon reasonable request.

Batteries & Supercaps

Research Article
doi.org/10.1002/batt.202500433

Chemistry Europe
European Chemical
Societies Publishing

[1] B. Ramasubramanian, J. Ling, R. Jose, S. Ramakrishna, *Cell Rep. Phys. Sci.* **2024**, *5*, 102032.

[2] R. Gonçalves, S. Lanceros-Méndez, C. M. Costa, *Electrochem. Commun.* **2022**, *135*, 107210.

[3] Y. Liu, R. Zhang, J. Wang, Y. Wang, *IScience* **2021**, *24*, 102332.

[4] J. Li, J. Fleetwood, W. B. Hawley, W. Kays, *Chem. Rev.* **2022**, *122*, 903.

[5] D. L. Wood, J. Li, C. Daniel, *J. Power Sources* **2015**, *275*, 234.

[6] M. Thomitzek, O. Schmidt, F. Röder, U. Krewer, C. Herrmann, S. Thiede, *Proc. CIRP.* **2018**, *72*, 346.

[7] D. Z. Dominguez, B. Mondal, M. Gaberscek, M. Morcrette, A. A. Franco, *J. Power Sources* **2023**, *580*, 233367.

[8] M. Titirici, P. Johansson, M. C. Ribadeneyra, H. Au, A. Innocenti, S. Passerini, E. Petavratzi, P. Lusty, A. A. Tidblad, A. J. Naylor, R. Younesi, Y. A. Chart, J. Aspinall, M. Pasta, J. Orive, L. M. Babulal, M. Reynaud, K. G. Latham, T. Hosaka, S. Komaba, J. Bitenc, A. Ponrouch, H. Zhang, M. Armand, R. Kerr, P. C. Howlett, M. Forsyth, J. Brown, A. Grimaud, M. Vilkman, K. B. Dermenci, et al., *J. Phys. Energy* **2024**, *6*, 041502.

[9] A. A. Franco, *RSC Adv.* **2013**, *3*, 13027.

[10] A. C. Ngandjong, A. Rucci, M. Maiza, G. Shukla, J. Vazquez-Arenas, A. A. Franco, *J. Phys. Chem. Lett.* **2017**, *8*, 5966.

[11] A. A. Franco, A. Rucci, D. Brandell, C. Frayret, M. Gaberscek, P. Jankowski, P. Johansson, *Chem. Rev.* **2019**, *119*, 4569.

[12] T. Lombardo, F. Lambert, R. Russo, F. M. Zanotto, C. Frayret, G. Toussaint, P. Stevens, M. Becuwe, A. A. Franco, *Batter. Supercaps* **2022**, *5*, e202200116.

[13] T. Lombardo, F. Caro, A. C. Ngandjong, J. B. Hoock, M. Duquesnoy, J. C. Delepine, A. Ponchelet, S. Doison, A. A. Franco, *Batter. Supercaps* **2022**, *5*, e202100324.

[14] M. Soori, B. Arezoo, R. Dastres, *Cogn. Rob.* **2023**, *3*, 54.

[15] S. O. Abioye, L. O. Oyedele, L. Akanbi, A. Ajayi, J. M. D. Delgado, M. Bilal, O. O. Akinade, A. Ahmed, *J. Build. Eng.* **2021**, *44*, 103299.

[16] T. Lombardo, M. Duquesnoy, H. El-Bouysidy, F. Åstrén, A. Gallo-Bueno, P. B. Jørgensen, A. Bhowmik, A. Demortière, E. Ayerbe, F. Alcaide, M. Reynaud, J. Carrasco, A. Grimaud, C. Zhang, T. Vegge, P. Johansson, A. A. Franco, *Chem. Rev.* **2022**, *122*, 10899.

[17] D. E. Galvez-Aranda, T. L. Dinh, U. Vijay, F. M. Zanotto, A. A. Franco, *Adv. Energy Mater.* **2024**, *14*, 2400376.

[18] D. E. Galvez-Aranda, F. Fernandez, A. A. Franco, *ACS Appl. Mater. Interfaces* **2025**, *17*, 32150.

[19] H. Tu, S. Moura, Y. Wang, H. Fang, *Appl. Energy* **2023**, *329*, 120289.

[20] T. H.-J. Uhlemann, C. Schock, C. Lehmann, S. Freiberger, R. Steinhilper, *Proc. Manuf.* **2017**, *9*, 113.

[21] M. N. Amiri, A. Håkansson, O. S. Burheim, J. J. Lamb, *Renewable Sustainable Energy Rev.* **2024**, *200*, 114577.

[22] E. Ayerbe, M. Berecibar, S. Clark, A. A. Franco, J. Ruhland, *Adv. Energy Mater.* **2022**, *12*, 2102696.

[23] I. Cardenas-Sierra, U. Vijay, F. Aguesse, N. Antuñano, E. Ayerbe, L. Gold, A. Naumann, L. Otaegui, N. Recham, S. Stier, S. Süß, L. Subramanian, N. Vallin, G. V. Silva, N. Von Drachenfels, D. Weitze, A. A. Franco, *J. Power Sources* **2025**, *631*, 236158.

[24] A. Mistry, A. A. Franco, S. J. Cooper, S. A. Roberts, V. Viswanathan, *ACS Energy Lett.*, **2021**, *6*, 1422.

[25] T. Lombardo, J. B. Hoock, E. N. Primo, A. C. Ngandjong, M. Duquesnoy, A. A. Franco, *Batter. Supercaps* **2020**, *3*, 721.

[26] A. E. Malki, M. Asch, O. Arcelus, A. Shodiev, J. Yu, A. A. Franco, *J. Power Sources Adv.* **2023**, *20*, 100114.

[27] D. P. Finegan, I. Squires, A. Dahari, S. Kench, K. L. Jungjohann, S. J. Cooper, *ACS Energy Lett.* **2022**, *7*, 4368.

[28] S. Kench, I. Squires, A. Dahari, F. B. Planella, S. A. Roberts, S. J. Cooper, *Matter* **2024**, *7*, 4260.

[29] J. F. Troncoso, F. M. Zanotto, D. E. Galvez-Aranda, D. Z. Dominguez, L. Denisart, A. A. Franco, *Batter. Supercaps* **2025**, *8*, e202400385.

[30] R. P. Cunha, T. Lombardo, E. N. Primo, A. A. Franco, *Batter. Supercaps* **2020**, *3*, 60.

[31] M. Duquesnoy, C. Liu, D. Z. Dominguez, V. Kumar, E. Ayerbe, A. A. Franco, *Energy Storage Mater.* **2023**, *56*, 50.

[32] A. Shodiev, M. Duquesnoy, O. Arcelus, M. Chouchane, J. Li, A. A. Franco, *J. Power Sources* **2021**, *511*, 230384.

[33] U. Vijay, D. E. Galvez-Aranda, F. M. Zanotto, T. Le-Dinh, M. Alabdali, M. Asch, A. A. Franco, *Energy Storage Mater.* **2025**, *75*, 103883.

[34] H. Zhang, S. Li, Y. Chen, J. Dai, Y. Yi, *Comp. Intell. Neurosci.* **2022**, *2022*, 5596676.

[35] M. Zhang, T. Z. Xiao, B. Paige, D. Barber, *arXiv preprint*, **2022**, arXiv:2205.14539.

[36] A. P. Thompson, H. M. Aktulga, R. Berger, D. S. Bolintineanu, W. M. Brown, P. S. Crozier, P. J. In T'Veld, A. Kohlmeyer, S. G. Moore, T. D. Nguyen, R. Shan, M. J. Stevens, J. Tranchida, C. Trott, S. J. Plimpton, *Comp. Phys. Commun.* **2022**, *271*, 108171.

[37] C. Sağlam, N. Çetin, *J. Food Proc. Preserv.* **2022**, *46*, e16496.

[38] Case Studies - GeoDict Simulation Software, (n.d.), (accessed March 2025), **2025**, https://www.math2market.com/geodict-software/geodict-applications.html.

[39] S. B. H. Ali, M. Alabdali, V. Viallet, V. Seznec, A. A. Franco, *J. Power Sources* **2025**, *630*, 236131.

[40] M. Chouchane, A. Rucci, A. A. Franco, *ACS Omega* **2019**, *4*, 11141.

[41] C. Liu, T. Lombardo, J. Xu, A. C. Ngandjong, A. A. Franco, *Energy Storage Mater.* **2023**, *54*, 156.

[42] M. Duquesnoy, C. Liu, V. Kumar, E. Ayerbe, A. A. Franco, *J. Power Sources* **2024**, *590*, 233674.

[43] J. Xu, A. C. Ngandjong, C. Liu, F. M. Zanotto, O. Arcelus, A. Demortière, A. A. Franco, *J. Power Sources* **2023**, *554*, 232294.

[44] J. Xu, B. Paredes-Goyes, Z. Su, M. Scheel, T. Weitkamp, A. Demortière, A. A. Franco, *Batter. Supercaps* **2023**, *6*, e202300371.